The Role of Small-scale Topography in Modulating Eddy Scale in the Northern South China Sea

Zhibin Yang[1], Zhao Jing[1, 2], and Xiaoming Zhai[3]

[1] Frontier Science Center for Deep Ocean Multispheres and Earth System (FDOMES) and Physical Oceanography Laboratory, Ocean University of China, Qingdao, China
[2] Laoshan Laboratory, Qingdao, China
[3] Centre for Ocean and Atmospheric Sciences, School of Environmental Sciences, University of East Anglia, Norwich, United Kingdom

Corresponding author: Zhao Jing, jingzhao198763@sina.com

Key Points:

- Adding small-scale topography leads to negligible changes to the surface eddy scales and their seasonal cycle
- The bottom eddy scales reduce by about 30-40% after adding small-scale topography
- This reduction in bottom eddy scales is contributed by wave generation, forward energy cascade and modification of deep boundary current

Abstract

A high-resolution nested model initialized with either smooth or synthetically-generated rough topography is used to investigate the role of small-scale topography in modulating eddy scales in the northern South China Sea. It is found that while adding small-scale topography leads to negligible changes in the surface eddy scales and their seasonal cycle, it significantly reduces the bottom eddy scales by about 30-40%. This reduction in bottom eddy scales is mainly contributed by three processes: wave generation due to flow interaction with rough topography and subsequent wave propagation into the ocean interior, forward energy cascade associated with processes such as nonpropagating form drag effect, and the influence of small-scale topography on the deep boundary current. Our results highlight the importance of small-scale topography in setting the eddy length scales particularly in the deep ocean.

Plain Language Summary

Oceanic eddies are an important component in the world's oceans. However, processes affecting the eddy length scales in the ocean are less well known. Here we investigate the role of small-scale rough topography in setting eddy scales in a high-resolution nested modelling system. We conduct two high-resolution ($\triangle x$ ~500 m) model experiments: a smooth topography experiment and a rough topography experiment. We find that the bottom eddy scales are significantly reduced whereas the surface eddy scales remain unchanged after adding small-scale rough topography.

1 Introduction

The ocean is intrinsically turbulent in nature and as a result of non-linear interactions energy in the ocean can transfer across spatial scales. Geostrophic turbulence theory predicts an inverse energy cascade (from small scales to large scales) of ocean eddy kinetic energy where the eddy length scale increases until it is halted at the Rhines scale by planetary wave propagation (Rhines, 1975; Salmon, 1998). However, satellite observations reveal that the dominate eddy scales in many regions of the oceans are only slightly larger than the local Rossby deformation radius (Stammer, 1997). This indicates that the inverse cascade is often arrested by other physical processes before it reaches the Rhines scale.

For example, Arbic and Flierl (2004) found that the bottom friction, or bottom drag, can arrest the inverse cascade and thereby modulate the eddy length scale. Eddies in their model simulations tend to have larger horizontal scales than observations under weak bottom drag. Another possible candidate process that can affect eddy scale is the generation of lee waves over small-scale topography (wave drag), which is believed to be an efficient way to cascade the mesoscale energy to small-scales that are more readily to be dissipated (Nikurashin et al., 2013). The downscale or forward eddy energy cascade (from large scales to small scales) above the small-scale rough topography may contribute to the arrest of inverse cascade and thereby reduce the eddy scales. However, the manner in which wave drag affects the eddy scales may be quite different from that of bottom drag. For example, different from the bottom drag which only occurs in the bottom boundary layer, lee waves can radiate away from the ocean bottom into ocean interior and interact with the mean flows (Baker & Mashayek, 2021; Kunze & Lien, 2019; Sun et al., 2022). In addition, existing literature (e.g., Nikurashin et al., 2013; Yang et al., 2021; Yang et al., 2022) found the presence of small-scale topography can prominently reduce the bottom velocity and further weaken the bottom drag, indicating that the role of bottom drag in modulating eddy scale could be overestimated in models that do not include small-scale topography.

Trossman et al. (2017) investigated the sensitivity of bottom drag and wave drag on flow baroclinicity in a global model with and without an internal wave drag parameterization. They showed that the presence of wave drag (or enhanced bottom drag) can enhance the flow baroclinicity, but has a negligible effect on the surface eddy scales. However, their result could be sensitive to the fixed vertical scale they prescribed for wave momentum flux distribution in their parameterization scheme (e.g., Saenko et al., 2012). The vertical scale is associated with the wave decaying processes (e.g., wave breaking; wave-flow and wave-wave interaction). Our understanding about these processes is limited (Whalen et al., 2020). In addition, the parameterization of wave drag is sensitive to model resolution (Hurlbut & Hogan, 2008; Ruan et al., 2021). Therefore, high-resolution lee wave resolving models are needed to test the sensitivity of small-scale topography in modulating ocean eddy scales.

The eddy length scale is a key parameter of ocean eddies and it matters for the role of the eddies play in the ocean such as in transporting and mixing tracers. As such, it is one of the key ingredients in the development of eddy parameterization schemes (e.g., Eden and Greatbatch, 2008; Visbeck et al., 1997). Here we want to investigate the potential candidates for modulating eddy scales, with a special focus on the generation of lee waves over small-scale topography. The eddy scales could be also associated with ocean energy cascade (Wang et al., 2019) and it may provide important clues in the precise estimate of the eddy dissipation coefficients near the ocean bottom and small-scale topography, which in turn, help us understand the larger-scale ocean circulation, such like the structure of deep-ocean western boundary current. The horizontal scale of radiating lee waves predicted by the linear theory ranges from $|U_b/f|$ to U_b/N (f and N are the Coriolis frequency and the bottom buoyancy frequency; U_b is the bottom velocity; Bell, 1975a, b), and typically spans a wavelength of ~O(0.1-10) km. We conduct two high-resolution ($\triangle x$ ~500 m) lee wave resolving ocean simulations of the northern South China Sea (SCS) to evaluate the role of small-scale topography in modulating eddy scales: one initialized with a smooth topography and the other one with a synthetically-generated rough topography. Strong mesoscale eddy activities have been found in the northern SCS and these eddies play a critical role in the biogeochemistry system of the SCS (Figure 1; Yang et al., 2019). In this study, we find the eddy scales are significantly reduced above the rough bottom whereas the surface scales remain unchanged. This paper is organized as follows. Model configuration is described in section 2. In section 3, we compare eddy scales in the two experiments and investigate the influence of small-scale topography on kinetic energy (KE) cascade. The reasons behinds the reduced eddy scales near the bottom and unchanged eddy scales at the surface are discussed in section 4. Results are summarized in section 5.

2 Methodology

2.1. Model configuration

A three-level nested modelling system (the Massachusetts Institute of Technology general circulation model (MITgcm); Marshall et al., 1997) is used in our study. The parent model (hereinafter P1) has a horizontal resolution of 1/24° covering most of the Northwest Pacific, and the two child models (hereinafter C1 and C2) have horizontal resolutions of 1/72° and 1/216°, respectively (Figure 1). A vertical resolution refinement (165 levels in total with maximum $\triangle z$ = 30 m) is also implemented in C1 and C2 to resolve the small-scale wave motions. All three models are driven by daily climatology forcing except for C2 which has a monthly wind forcing to avoid the wind-induced near-inertial waves. No geothermal heating or tide forcing is included in any of the model runs. Detailed model configurations can be found in Yang et al. (2022) where the same model configuration was used to study the effect of rough topography on eddy dissipation in the northern SCS. We evaluated the C1 model performance by comparing the model-simulated eddy KE with that derived from the satellite-observed sea level anomaly data and found they compare well. We also compared the model buoyancy frequency and bottom velocity (two important parameters determining whether the lee waves radiate or not) with World Ocean Atlas climatology and data-assimilated reanalyses products (ECCO2), and found that both parameters in our model match the observation and reanalysis data reasonably well (Yang et al., 2022).

Two experiments are designed in the C2 simulation: one with a smooth topography (hereafter SMOOTH) and the other with a rough topography (hereafter ROUGH). The smooth topography is obtained from the SRTM30_PLUS dataset (Becker et al., 2009) which is smoothed using a spatial low-pass filter with a cutoff wavelength of 20 km which eliminates the radiation of most of the lee waves (Bell, 1975a, b). Moreover, synthetic small-scale (<20 km) topography is added to the smoothed topography, but only to regions deeper than 500 m to avoid outcropping of the superimposed topography in ROUGH experiment. The synthetic topography (Figure A1) is derived from the topographic spectral model of Goff and Jordan (1988):

$$P(k,l)=\frac{2\pi h^2(\mu-2)}{k_0 l_0}\times\left[1+\frac{k^2}{k_0^{\ 2}}\cos^2(\phi-\phi_0)+\frac{l^2}{l_0^{\ 2}}\sin^2(\phi-\phi_0)\right]^{-\mu/2}. \qquad (1)$$

The characteristic wavenumbers (k_0, l_0), the variance of the topographic height (h^2) and the slope of high-wavenumber roll-off (μ) are derived from observed single beam topographic data by fitting the spectral parameters in Eq. (1). Here we assume the synthetic topography is isotropic without considering the wave vector angle (ϕ) and the azimuthal angle (ϕ_0). Then the synthetic topography is generated as a sum of Fourier modes with same amplitudes given by the topographic spectrum but with random phases. This method for generating synthetic topography has been widely used in studies of internal tides (e.g., Melet et al., 2013; Nikurashin & Legg, 2011) and lee waves (e.g., Nikurashin et al., 2013; Yang et al., 2021). Detailed method for the synthetic topography generation can be found in APPENDIX C of Yang et al. (2022).

The two experiments have been run for 26 months and the model outputs of the last 20 months will be analyzed in this study. Both the upper- and bottom-ocean KE are found to reach quasi-equilibrium states after 6 months, with the annual drift of KE being less than 3% of the total KE in both experiments (Yang et al., 2022). A region 2° away from the nesting boundary of C2 simulation is chosen for analysis in this study (dashed white line in Figure 1).

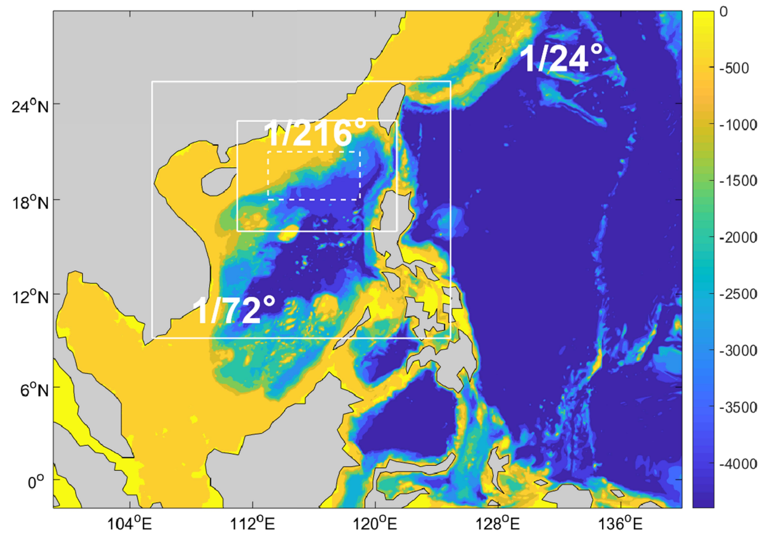

Figure 1. Bathymetry (m) used in the parent model. The white solid lines represent the boundaries of the nested models. The study region is delineated by the white dashed line (section 3).

2.2. Vorticity integral scales

We use a vorticity integral scale (L_v) to evaluate the eddy scale which captures the average horizontal scale of vortical features (Srinivasan et al., 2019):

$$\frac{1}{L_v} = \frac{1}{2\sqrt{2}} \left(\frac{\int \zeta^2 dV}{\int \mathrm{KE}\, dV} \right)^{1/2}, \tag{2}$$

where $\zeta = v_x - u_y$ is the vertical vorticity and $\mathrm{KE} = \left(u^2 + v^2\right)/2$ is the kinetic energy. Note that the total velocity used in Eq. (2) also includes small-scale wave motions. In this study we mainly focus on the length scale of the “balanced” eddy motions with the “unbalanced” referring to wave motions (Torres et al., 2018). We will discuss the contribution of wave motions to L_v in section 3.3.

2.3. KE dissipation

The KE is dissipated by the bottom friction (ε_b):

$$\varepsilon_b = C_d \left| \mathrm{u}_b \right|^3, \tag{3}$$

and the interior viscous dissipation (ε_v):

$$\varepsilon_v = A_h\left[\left(\frac{\partial \mathbf{u}_h}{\partial x}\right)^2 + \left(\frac{\partial \mathbf{u}_h}{\partial y}\right)^2\right] + A_{4h}\left(\nabla_h^{\,2}\mathbf{u}_h\right)^2 + A_z\left(\frac{\partial \mathbf{u}_h}{\partial z}\right)^2 \quad (4)$$

C_d is the quadratic drag coefficient. A_h and A_{4h} are the harmonic and bi-harmonic horizontal viscosity coefficients. A_z is the vertical viscosity coefficient. $\mathbf{u}_h$ is the horizontal velocity. Note that dissipation caused by wave drag is included in ε_v.

2.4. Decomposition of wave and nonwave motions

The intrinsic phase speed of internal lee waves is equal and opposite to the flow so that they are stationary in an Eulerian frame (Nikurashin & Ferrari, 2010). Here we decompose the velocity field in a Lagrangian frame which accounts for the Doppler shifting of wave frequency (Nagai et al., 2015; Shakespeare & Hogg, 2017; Yang et al., 2021; Yang et al., 2022). The wave motion is isolated by filtering the motions with Lagrangian frequencies higher than f.

Nearly 150 million flow-following floats (one float per model cell) are introduced in the two experiments and their trajectories are saved hourly over 2-day simulated periods. These 2-day periods are chosen because the volume-integrated energy dissipation during these 2 days is close to their annual average. The lee wave KE is mainly concentrated above the rough bottom and is weak in the upper 300 m (Yang et al., 2022). To reduce computational cost, particles in the SMOOTH experiment are only introduced in the water column below 300 m depth. We first use a high-pass filter (higher than f) on the float velocity fields and then interpolated the filtered velocity back to the model grid. The wave velocity ($\mathbf{u}_w$) and nonwave velocity ($\mathbf{u}_{nw}$) are defined as the interpolated high-frequency (low-frequency) velocity, respectively. The KE viscous dissipation associated with wave and nonwave motions can then be calculated using Eq. (4) with $\mathbf{u}_w$ and $\mathbf{u}_{nw}$, respectively. Detailed method description can be found in Yang et al. (2022).

2.5. Cross-scale eddy kinetic energy flux

We use a coarse-graining method to calculate the cross-scale kinetic energy fluxes (CSF) in the two experiments (Eyink & Aluie, 2009). Different from the conventional methods of spectral flux (e.g., Arbic et al., 2013; Capet et al., 2008), the advantage of this method is that it can deal with the small-scale inhomogeneous flows (e.g., lee waves in our study; Aluie et al., 2018).

The CSF can be diagnosed as follows:

$$\Pi(\ell) = \Pi_h(\ell) + \Pi_z(\ell), \quad (5)$$

where

$$\Pi_h(\ell) = -\left[\left(\overline{u^2} - \bar{u}^2\right)\bar{u}_x + \left(\overline{uv} - \bar{u}\bar{v}\right)\left(\bar{u}_y + \bar{v}_x\right) + \left(\overline{v^2} - \bar{v}^2\right)\bar{v}_y\right], \quad (6)$$

and

$$\Pi_z(\ell) = -\left[\left(\overline{vw} - \bar{v}\bar{w}\right)\bar{v}_z + \left(\overline{uw} - \bar{u}\bar{w}\right)\bar{u}_z\right]. \quad (7)$$

The overbars in Eqs. (6-7) represent the low-pass filtering (with a cutoff scale ℓ) with convoluted filters. Positive (Negative) $\Pi(\ell)$ represents a downscale (upscale) energy transfer.

$\Pi(\ell)$ with length scales ℓ=3, 5, 10, 15, 20, 35, 50, 70 km are calculated both in SMOOTH and ROUGH experiments.

3. Results

3.1. Eddy scales

The surface and bottom eddy scales are first calculated in SMOOTH and ROUGH experiments (only regions deeper than 500 m are considered, i.e., regions superimposed by rough topography; Figure 2). The eddy scales are computed using Eq. (2) for different surface and bottom layers. Figures 2a, b show the diagnosed eddy scales averaged in the surface 50 m and surface 200 m of the two experiments in the last 20 months. The surface eddy scales in both experiments exhibit a similar strong seasonal cycle with larger scales in summer and smaller scales in winter. The main difference between eddy scales in the surface 50 m and those in the surface 200 m appears in winter, with slightly larger scales in the surface 200 m (~30 km in the surface 50 m vs. ~40 km in the surface 200 m). The northern SCS is characterized by energetic submesoscale motions in winter which are mainly associated with the mixed-layer instability (Zhang et al., 2020). Figure 3 shows the simulated surface Rossby number (ζ/f) on July 18th and January 18th, respectively. On a typical summer day (Figures 3a, c), large Rossby numbers occur only at the edge of mesoscale eddies, whereas on a winter day (Figures 3b, d), significant submesoscale motions with large Rossby numbers can be spotted almost in the whole northern SCS. The submesoscale motions with horizontal scales of O(1-10 km) can modulate the vorticity integral eddy scales, resulting in smaller L_v in winter (Qiu et al., 2014). Quantitatively, the root-mean-square of the Rossby number is 0.60 (0.61) for SMOOTH (ROUGH) in winter and 0.18 (0.19) in summer. The seasonal variation of the Rossby numbers is much greater than that of the surface eddy scales (Figures 2a-b) because the former is more dominated by the submesoscale activities, which, however, only account for a small part of ocean energy (Zhang et al., 2021). In addition, the submesoscale activities are mainly concentrated within the surface mixed layer (the mixed layer depth of the northern SCS in winter is typically about 50 m), resulting in a slightly smaller eddy scale in the surface 50 m than that in the surface 200 m in winter.

There are no obvious differences in eddy scales in the surface layers between the two experiments, consistent with the model result of Trossman et al. (2017) where the bottom wave drag is parameterized. We also calculate energy-containing scales associated with the power spectral density of KE ($L_c = \dfrac{\iint \widetilde{E}(k,l)dkdl}{\iint \sqrt{k^2+l^2}\,\widetilde{E}(k,l)dkdl}$ where $\widetilde{E}(k,l)$ denotes the power spectral density of KE) averaged in the top 50 m and find similar annual-mean and seasonal cycle of eddy scales in the two experiments (not shown). However, applying this energy spectral method to diagnose energy-containing eddy scales near the bottom is challenging due to the presence of topography.

In contrast, there is no discernible seasonal cycle of eddy scales near the bottom and the eddy scales in ROUGH are significantly smaller than those in SMOOTH (Figures 2c, d). Quantitatively, the average eddy scale in the bottom 100 m (300 m) is 4.4 km (7.2 km) in the SMOOTH experiment, compared to 3 km (4.9 km) in the ROUGH experiment, representing a decrease of 32% (32%).

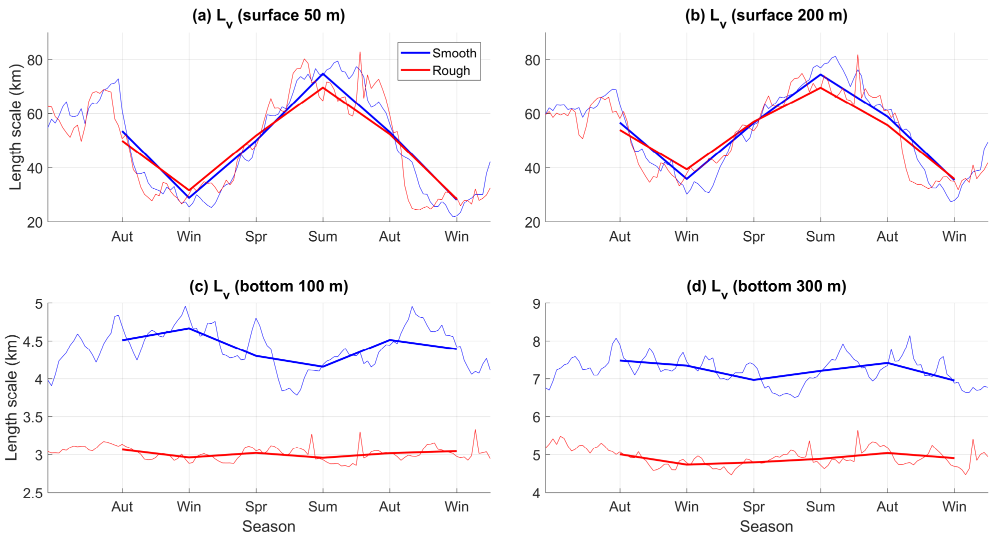

Figure 2. Time series of eddy scales (Eq. (2), L_v, km) averaged in the top (a) 50 m and (b) 200 m and in the bottom (c) 100 m and (d) 300 m in the two experiments. Thin blue (red) lines represent instantaneous results with an interval of 5 days for SMOOTH (ROUGH), and the thick lines represent their seasonal averages.

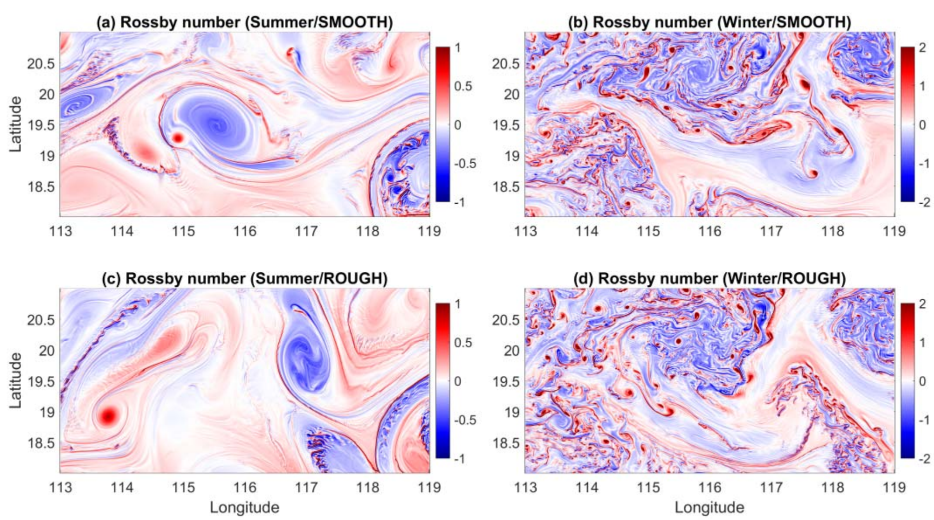

Figure 3. Spatial distributions of surface Rossby number (ζ/f) on (a, c) July 18th and (b, d) January 18th. (a, b) Results from the SMOOTH experiment and (c, d) results from the ROUGH experiment. Only the results in the study region are shown (white dashed line in Figure 1).

Given that the average eddy scale in the bottom layer is significantly smaller in ROUGH than in SMOOTH but they are comparable in the surface layers, it is of interest to find out the vertical scale of the influence of rough topography on eddy scales. To do that, we calculate the volume-averaged eddy scales with similar water depths and composite eddy scales according to the depth of the SMOOTH topography (Figures 4a, b). Detailed methods are as follows: all grids are re-arranged according to the depth of the SMOOTH topography; then grids with similar depths (e.g., 0-250 m; 250-500 m; 500-750 m...) are grouped together; in each group, we calculate the volume-averaged eddy scales within a vertical bin of 250 m (from top to bottom).

In this study, we use the SMOOTH topography as the reference topography and regard the height above/below the SMOOTH topography (i.e., HAB > 0 and HAB <0) as the 'crest' and 'trough' of the rough topography (note the average depth of the added small-scale topography is 0 m). In both experiments the eddy scales are found to gradually decrease with depth from over 50 km near the surface to about 10 km near the bottom. Only slight differences in eddy scales exist in the upper ocean between the two experiments. In addition, the eddy scales in ROUGH are about 30-40% smaller compared to SMOOTH within several hundred of meters (about 500 m in the slope region but more than 1000 m in the deep basin) above the rough topography. No such scale difference can be found near the bottom in the shelf region (shallower than 500 m) where small-scale topography is not added.

Even though the bottom eddy scales only differ by about several kilometers between the two experiments, the percentage difference is large (about 30-40%) within a few hundred meters over the rough topography because the eddy scales are small there. The reduced bottom eddy scales in ROUGH may have implications for eddy energy dissipation. Our previous study (Yang et al., 2022) has found significantly enhanced viscous dissipation within hundreds meters over the rough bottom. Here we reproduce the result of viscous energy dissipation rates in Figures 4d-f. There is a band of elevated viscous dissipation close to the rough topography and also further up in the water column. The areas of enhanced viscous dissipation generally coincide with the areas of reduced eddy scales in ROUGH. The close connection between the viscous dissipation and reduced bottom eddy scales suggests an enhanced downscale energy cascade in the ROUGH experiment which we will discuss in details in section 3.2.

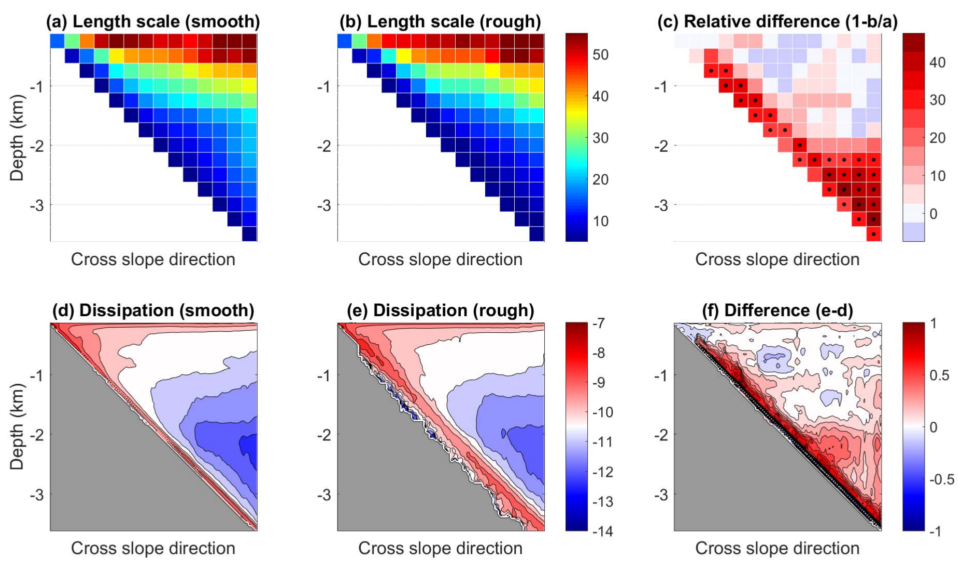

Figure 4. (a-b) Time-mean composite eddy scales (Eq. (2), L_v, km) in SMOOTH and ROUGH (km) and (c) their relative difference (percentage). (d-e) Composited viscous dissipation (Eq. 4, in $\log_{10}$, W/kg) in SMOOTH and ROUGH and (f) their relative difference. Black dots in (c) indicate percentage differences greater than 25%.

3.2. Cross-scale kinetic energy flux

To evaluate the impact of rough topography on energy cascade in our model simulations, we compute the CSF ($\Pi(\ell)$) with a coarse-graining method (Eyink & Aluie, 2009).

Figure 5 shows the CSF in the surface layer in summer and winter in the two experiments. Seasonal changes of CSF are mostly confined in the upper ocean with a larger amplitude in winter than in summer. In the top 20 m and particularly in wintertime, the CSF is positive, i.e., energy flux is downscale, which is in contrast with some previous modelling studies (e.g., Dong et al., 2020; Sasaki et al., 2014; Schubert et al., 2020) where the dominant energy transfer is found to be from submesoscales to mesoscales, i.e, upscale energy flux. A possible explanation for this discrepancy is the much higher model resolution used in this study (~500 m) compared to previous studies, e.g., ~3km in Sasaki et al. (2014). Recent open ocean observations by Naveira Garabato et al. (2022) found a downscale energy transfer from mesoscale to submesoscale motions as a result of frontogenesis processes. However, models with resolution fine enough to resolve mixed layer instability still fail to reproduce this frontal downscale energy transfer due to resolution limit. Here we repeat the calculation of the CSF in the middle-level nested model, i.e., C1, which has a horizontal resolution three times coarser than C2 used for SMOOTH and ROUGH experiments. The CSF in the surface layer of C1 is found to be much less positive than that in C2. For example, the positive summer CSF in C2 now disappears in C1 and the winter CSF in C1 is negative at scales larger than ~45 km (Figure B1). Below the surface 20 m or so, the CSF are directed toward larger scales (negative), consistent with the geostrophic turbulence theory which suggested a 'inverse cascade' of KE (Salmon, 1998). The differences in CSF between the two experiments are very small, consistent with the similar surface eddy scales found in the two experiments (Figures 2a, b).

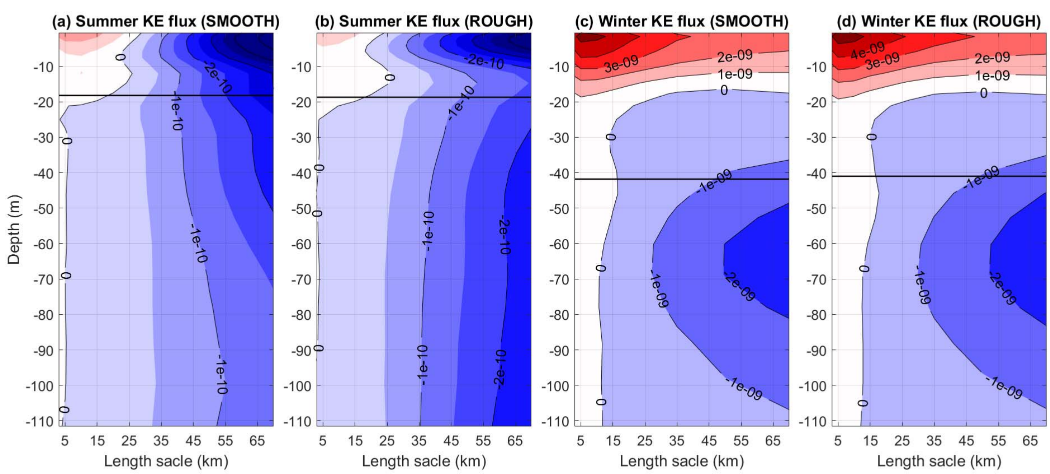

Figure 5. Time-mean surface cross-scale kinetic energy fluxes (Eqs. (5-7), $\Pi(\ell)$, W/kg) in (a-b) summer (JJA) and (c-d) winter (DJF). (a) and (c) are results for the SMOOTH experiment whereas (b) and (d) for the ROUGH experiment. Positive (Negative) shading indicates a forward (inverse) energy cascade. Black lines show the locations of the mixed layer (0.2^{o}C temperature difference with surface).

Unlike the surface CSF, the bottom CSF show significant differences between the two experiments (Figure 6). In the SMOOTH experiment, the inverse energy transfer takes place almost everywhere, except for very close to the bottom where a forward energy transfer occurs at relatively small scales (<25 km). Note that the lee waves can still be generated in SMOOTH, especially in the shallow bottom where the bottom velocity is relatively strong, which contributes to the forward energy transfer seen in SMOOTH. In the ROUGH experiment, although the ocean interior is still characterized by inverse cascade (upscale), the upscale energy flux is weaker compared to that at the same depth in the SMOOTH experiment. In addition, a much more substantial downscale energy transfer occurs both at small scales and large scales within the bottom 200 m above the rough bottom. The thickness of this bottom layer of downscale energy transfer is close to that of the band of bottom-enhanced dissipation shown in Figure 4f.

The slope of CSF, $T(\ell)=\partial\Pi(\ell)/\partial\ell$, implies sources or sinks of eddy KE for different length scales. Negative values of $T(\ell)$ (divergence) indicate an energy source for eddy KE at scale ℓ while positive values (convergence) represent an energy sink at scale ℓ. Here we define a convergence scale for the inverse cascade ($\partial\Pi(\ell)/\partial\ell=0$) which has been used to indicate the surface eddy scale in the Agulhas region (Schubert et al., 2020). The convergence scale is found to be about 20 km in the SMOOTH experiment, but 10-15 km in the ROUGH experiment (yellow lines in Figure 6). The smaller convergence scale in the ROUGH experiment shows that the inverse cascade is arrested at smaller scales and further contribute to the reduced bottom eddy scales found in ROUGH.

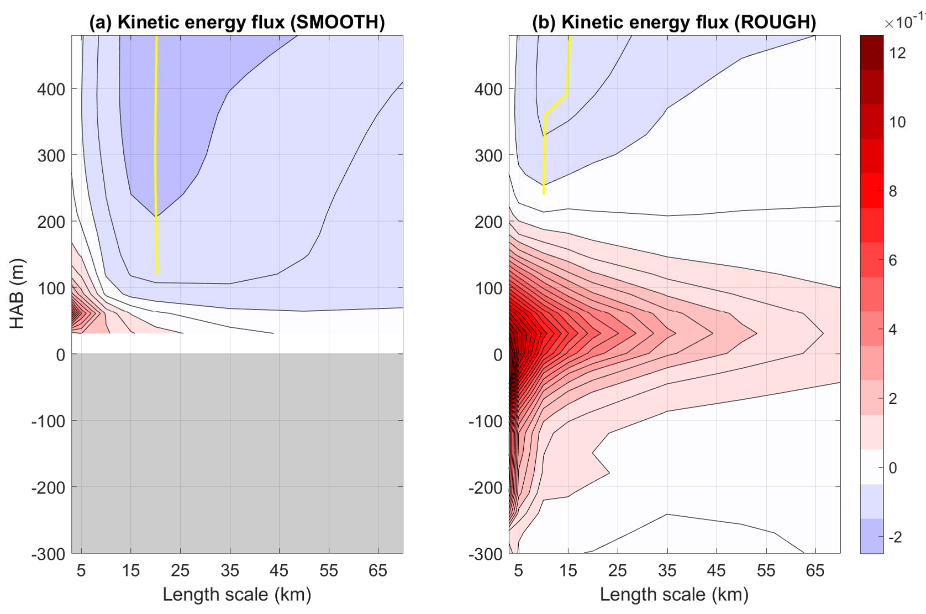

Figure 6. Time-mean bottom cross-scale kinetic energy fluxes (Eqs. (5-7), $\Pi(\ell)$, W/kg) in (a) SMOOTH and (b) ROUGH. Positive (Negative) shading indicates a forward (inverse) energy cascade. The yellow lines mark the convergence scales ($\partial\Pi(\ell)/\partial\ell=0$).

3.3. Wave and non-wave contributions

The horizontal scale of the radiating lee wave predicted by the linear theory typically spans a wavelength of ~O(0.1-10) km (Bell, 1975a, b). Previous studies (e.g., Nikurashin et al., 2013; Polzin et al., 1997; Yang et al., 2022) found that the internal wave energy is strongly enhanced above the small-scale topography. Further analyses are therefore required to determine whether the reduction of eddy scales seen in ROUGH is associated with the small-scale wave motions or due to the reduced scales of balanced eddy motions. We quantify the influence of small-scale wave motions on L_v by isolating the wave motions using the Lagrangian filtering method. Eddy scales associated with the nonwave motions alone are then computed using Eq. (2) with $\mathbf{u}_{nw}$.

Figure 7 shows the composited eddy scales calculated with the total velocity and with the nonwave velocity alone in the two experiments (on May 13rd for SMOOTH and on May 23rd for ROUGH). After isolating the wave motions, both SMOOTH and ROUGH experiments show an increase in eddy scales, especially close to the bottom. In SMOOTH, large differences are mainly concentrated in the upper slope region where they can exceed 10% and the differences elsewhere (deeper than 2000 m) are mostly less than 5% (Figure 7a-c). This spatial pattern is consistent with the distribution of wave energy in the SMOOTH experiment which shows a bottom enhancement only above the shallow slope (Figure 8a). The shallow regions typically have stronger bottom velocities, which could lead to internal wave generation (between horizontal scales from $|U_b/f|$ to U_b/N) despite of the absence of small-scale (<20 km) topography in the SMOOTH experiment. In ROUGH experiment, the eddy scales calculated with the nonwave velocity alone are greater than those calculated with the total velocity, particularly above the rough topography where the relative differences can be as large as 20% on the shallow slope and about 15% in the deep basin (Figure 7d-f). In the ocean interior, the eddy scales also increase by 5-10% after the wave motions have been excluded.

Although the presence of wave motions in ROUGH reduces the eddy scales diagnosed from the total velocity, especially close to the ocean bottom, it only partly explains the differences in eddy scales found between SMOOTH and ROUGH. After removing the wave motions, the bottom eddy scales associated with nonwave motions are still found to be about 20% smaller in ROUGH than SMOOTH. For example, the average nonwave eddy scale in the bottom 100 m (300 m) is 4.5 km (8.7 km) in the SMOOTH experiment comparing to 3.5 km (6.8 km) in the ROUGH experiment, representing a difference of 22% (22%). Figure C1 shows the nonwave eddy scale differences between the two experiments (i.e., Figure 7b minus Figure 7e). The bottom nonwave eddy scales are generally larger in SMOOTH, especially in the shallow slope region and deep basin. In the ocean interior, the eddy scales in SMOOTH are larger above the shallow slope and deep basin, but smaller in other regions. This may be because the 2-day Lagrangian wave analysis periods is short. This result indicates that other physical processes at work are responsible for the reduced eddy scales associated with balanced motions in ROUGH which we will discuss in section 4b.

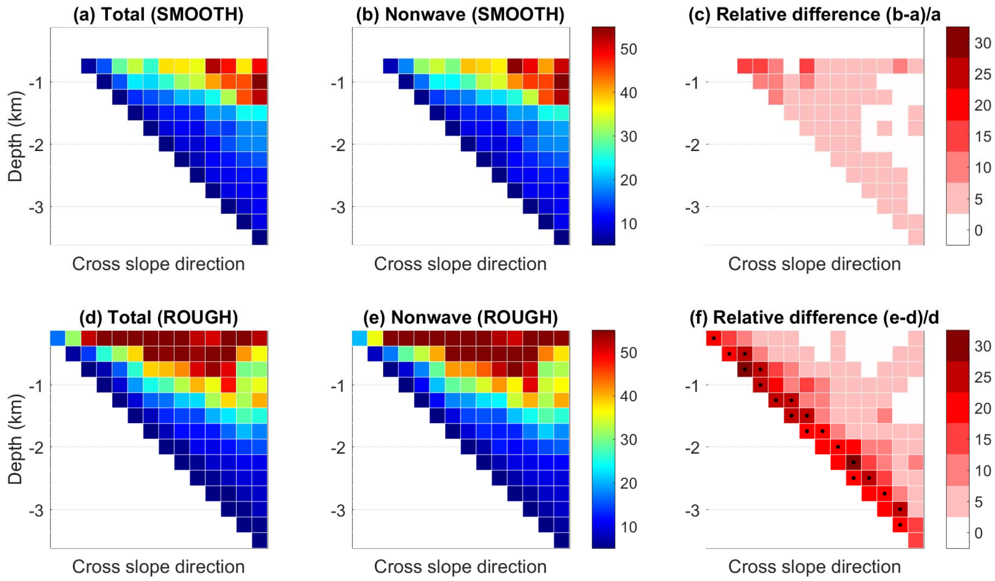

Figure 7. Composite eddy scales (Eq. (2), L_v, km) calculated with (a, d) the total velocity and (b,e) the nonwave velocity and (c, f) their relative differences (percentage) averaged over the 2-day periods (May 12nd-13rd for SMOOTH and May 22nd-23rd for ROUGH) when a Lagrangian filter method is used to isolate wave motions. (a-c) Results from the SMOOTH experiment and (d-f) results from the ROUGH experiment. To reduce the computational cost, particles in the SMOOTH experiment are only introduced in the water column below 300 m depth (surface white areas in a-c). Black dots in f indicate percentage differences greater than 20%.

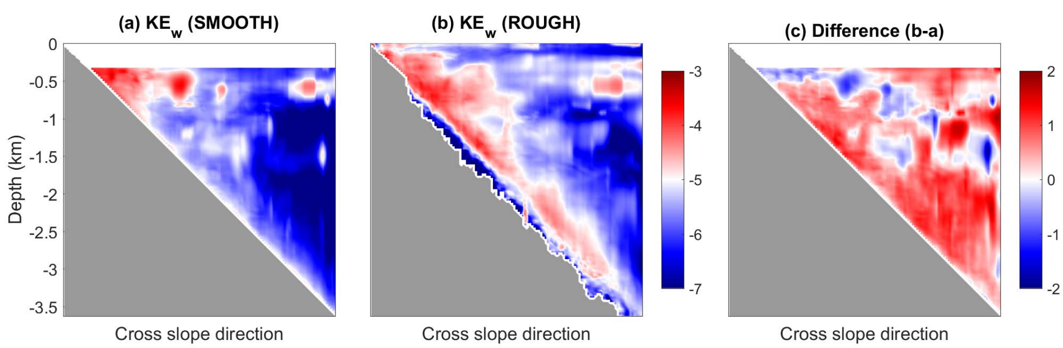

Figure 8. Composite distribution of wave KE (in $\log_{10}$, m^2/s^2) in (a) SMOOTH and (b) ROUGH over the 2-day Lagrangian wave analysis periods and (c) their difference (in $\log_{10}$, m^2/s^2).

The CSF diagnosed in the previous section also includes the wave process such as mean-to-wave conversion (MTW conversion). In order to isolate energy cascade associated with balanced eddy motions, we now calculate the nonwave CSF using the nonwave component $\mathbf{u}_{nw}$ in Eqs. (5-7) (Figure 9).

The total CSF averaged over the 2-day Lagrangian wave analysis periods is similar to the time-mean CSF in the two experiments: significant downscale energy transfers can be found within the 200 m above the rough topography in ROUGH whereas they only occur at small scales and very close to the bottom in SMOOTH (Figures 9a, d). After excluding the wave motions, the bottom downscale KE fluxes disappear in SMOOTH. Although the bottom downscale KE fluxes are greatly reduced in ROUGH, there are still significant downscale energy fluxes at small scales, highlighting the role of nonwave processes in energy transfers above the rough topography. In the ocean interior, the nonwave CSF is responsible for the majority of the inverse cascade seen in the total CSF (Figures 9b, e). The differences between the total and the nonwave CSF are most likely associated with the MTW energy conversion (Figures 9c, f). In our previous study (Yang et al., 2022), we calculated the MTW energy conversion terms following Shakespeare and Hogg (2017) and found large values of positive MTW (from nonwave to the lee wave field) occur mainly in the bottom 200 m. Here we find the CSF below 200 m in ROUGH can be as large as 10^{-10} W/kg which is of the same order of magnitude as the MTW diagnosed in Yang et al. (2022).

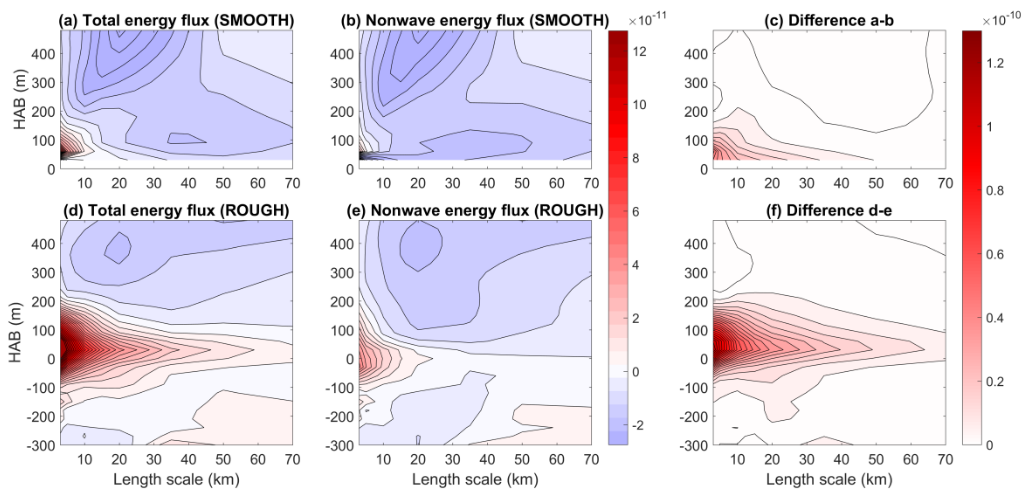

Figure 9. Bottom cross-scale kinetic energy fluxes (Eqs. (5-7), a&d) and their nonwave components (with nonwave velocity in Eqs. (5-7), b&e; W/kg) in (a-c) SMOOTH and (d-e) ROUGH averaged over the 2-day Lagrangian wave analysis periods. Positive (Negative) shading indicates a forward (inverse) energy cascade. (c&f) Differences between the total cross-scale energy fluxes and their nonwave components (W/kg).

3.4. Ocean baroclinicity

Our results suggest the presence of rough topography leads to significant downscale eddy energy cascade above the rough topography which may further enhance the baroclinicity of the ocean. Following Trossman et al. (2017), here we quantify the flow baroclinicity using two methods (Figure 10). The first method uses the ratio of baroclinic to barotropic KE (i.e., KE_{bc}/KE_{bt}). We define the barotropic velocity as the depth-averaged velocity and the baroclinic velocity as the deviations from the barotropic velocity. The second method uses the ratio of surface (100 m) to bottom (300 m) KE (i.e., $KE_{top100}/KE_{bottom300}$). Using different surface or bottom thicknesses will not change our results.

Both measurements show larger ratios in the ROUGH experiment, especially in the deep basin region (deeper than 3000 m; Figure 10, Table 1), indicating an enhancement of ocean baroclinicity in the presence of rough topography. $KE_{top100}/KE_{bottom300}$ shows a more significant enhancement in ROUGH than KE_{bc}/KE_{bt}. The former increases almost everywhere in the

ROUGH experiment whereas the later only becomes larger in the deep basin region (Table 1). One possible explanation is that our experiments are not in the weak drag limit. The former method is found to be more suitable to quantify the flow baroclinicity when bottom drag is weak while the later is more suitable when bottom drag is strong (Arbic & Flierl, 2004).

We also compare the sea surface height variance and time-average surface KE between the two experiments, but there is no obvious difference between them. It seems that in addition to the unchanged surface eddy scales, other parameters of the upper ocean are also insensitive to the small-scale topography in our model experiments. This provides another reason for the smaller difference in KE_{bc}/KE_{bt} between SMOOTH and ROUGH, since KE_{bc} is surface-intensified and the difference in KE_{bt} between the two experiments is relatively small (Table 1).

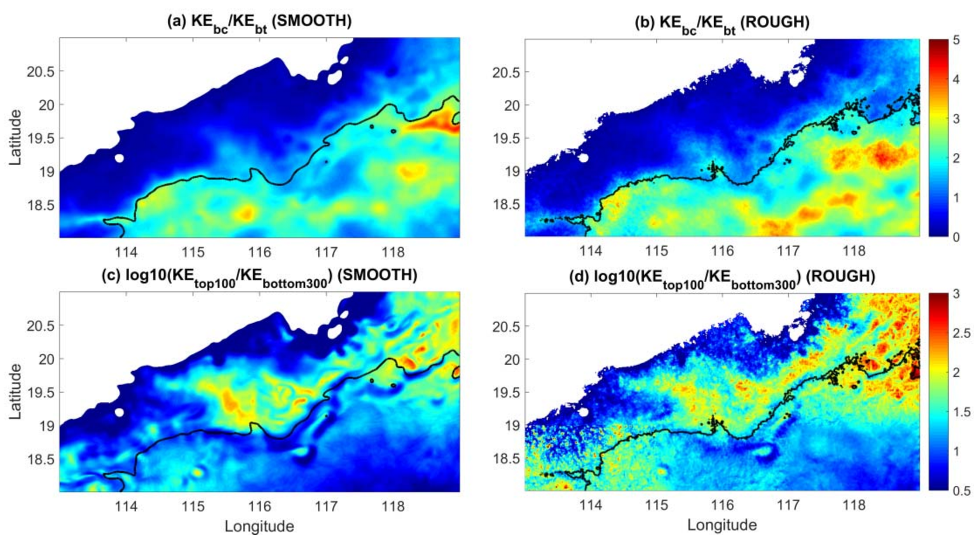

Figure 10. Measurements of ocean baroclinicity in the two experiments. Ratio of baroclinic to barotropic KE (KE_{bc}/KE_{bt}) in (a) SMOOTH and (b) ROUGH experiments. Ratio of near surface (top 100 m) to near bottom (bottom 300 m) KE (in $\log_{10}$) in (c) SMOOTH and (d) ROUGH experiments. The black solid line shows the 3000-m isobath. Only regions deeper than 500 m are shown.

Table 1. The area-weighted average of KE_{bt}, KE_{bc}/KE_{bt} and $KE_{top100}/KE_{bottom300}$ in SMOOTH and ROUGH experiments. Slope: 500-3000 m; basin: deeper than 3000 m. Values in bold fail to pass the significance test.

	SMOOTH			ROUGH		
	Slope	Basin	Total	Slope	Basin	Total
KE_{bt} ($\times 10^{-3}$ m^2/s^2)	4.0	0.79	2.5	3.7	0.63	2.3
KE_{bc}/KE_{bt}	**0.71**	2.11	1.35	**0.72**	2.44	1.51
$KE_{top100}/KE_{bottom300}$	28.7	16.6	23.2	50.2	35.7	43.5

4. Discussion

a. Surface eddy scales unchanged

We find the surface eddy scales remain unchanged in the presence of the small-scale topography. Trossman et al. (2017) also found similar results in a global model with parameterized wave drag and they hypothesized a short-circuiting of barotropization in the presence of the wave drag. A possible explanation is that the enhanced viscous dissipation owing to the small-scale topography is largely compensated by the reduction in bottom friction in ROUGH[1] (Yang et al., 2022). For example, the volume-integrated (below 300-m depth) viscous dissipation is found to be enhanced by 73% in ROUGH compared to SMOOTH (31.45 W vs. 54.47 W) whereas the volume-integrated bottom friction is reduced by 33% (39.2 W vs. 26.36 W). The reduced bottom friction tends to increase the horizontal eddy scale which may counteract the effect of wave drag (Arbic & Flierl, 2004). In addition, the large stratification in the upper ocean may also play a part in maintaining the surface eddy scales. It has been found that the surface-intensified stratification could arrest the inverse cascade (Arbic & Flierl, 2004). Note that the surface stratification of the two experiments are quite similar.

---

[1] We find the dominant sink of lee wave energy in our model is wave dissipation (Yang et al., 2023), although recent studies (e.g., Kunze & Lien, 2019; Wu et al., 2022) suggest the lee wave energy absorption by bottom-intensified flows may be also important for the lee wave energy sink.

b. Nonwave processes

The reduced eddy scale above the rough topography could be associated with wave motions generated by flow-topography interaction, such as internal waves and inertial oscillations. However, we find the bottom eddy scales associated with nonwave motions are also reduced by about 20% in the ROUGH experiment. In addition, there are significant forward cross-scale nonwave energy transfers in the ROUGH experiment, whereas they are hardly seen in the SMOOTH experiment. These results indicate that nonwave processes also contribute to the reduced eddy scales found in ROUGH.

In our previous work (Yang et al., 2022), we have found the presence of rough topography significantly enhances viscous dissipation and instabilities (e.g., anticyclonic-ageostrophic instability, symmetric instability) within hundreds meters above the rough bottom. Among this enhanced viscous dissipation, only one third is caused by the enhanced wave energy dissipation, whereas the remaining two thirds is explained by an enhancement of the nonwave dissipation which is associated with the nonpropagating form drag effect (Klymak, 2018). The importance of the nonpropagating form drag effect was also highlighted by Trossman et al. (2015). For weak near-bottom flow or large-amplitude medium-scale topography (consistent with the rough topography simulation), the bottom flow is inherently turbulent. In this situation, the nonpropagating form drag could be a more efficient route to energy dissipation than the wave radiation. Including the small-scale topographic features in ROUGH experiment could not only significantly weaken the near-bottom flow, but also increase the topography amplitude. Both effects tend to enhanced the nonpropagating form drag. The nonpropagating form drag effect can be also inferred from the composite distribution of KE (Figures 11c-d). Below the SMOOTH topography (i.e., HAB < 0), the KE in ROUGH is significantly reduced due to the blocking effect. The nonwave processes, such as submesoscale instabilities and the nonpropagating form drag effect, could be efficient routes for transferring energy to small-scale motions and be responsible for the reduced nonwave eddy scales found in ROUGH.

c. Reduced eddy scales in the ocean interior

It's interesting to see that the reduction of eddy scales extend more than 1000 m into the ocean interior above the rough bottom in the deep basin (Figure 4c), given that both wave generation and nonwave processes occur close to the rough bottom. This large vertical scale may be associated with the propagation of wave motions into the ocean interior since the area of reduced eddy scales generally coincides with the area of large wave KE differences (Figure 8c). However, this is not the only physical process at work because the interior eddy scales are still reduced in ROUGH compared to SMOOTH after the wave motions are excluded (Figures 5b, e).

In our model, a bottom-intensified deep western boundary current is constrained between the 3000- and 3500-m isobath in the northern SCS, consistent with previous model result (e.g., Zhao et al., 2020; Figure 11). However, the horizontal mean flows in the deep ocean are quite different between the two experiments. The deep current in SMOOTH has a more spatially-coherent structure with an average speed of about 1 cm/s, whereas the deep current in ROUGH is much weaker, narrower and less continuous own to the superposition of rough topography.

In our analysis so far the eddy scales are calculated using Eq. (2) with the total velocity since the mean flow is usually much weaker than the “eddy flow”. However, this assumption may not be true for the intensified boundary current. The reduction in eddy scales in the ocean interior could be overestimated due to the differences in the scales of the mean flow between the two experiments. To test this hypothesis, we compute and compare the eddy scales diagnosed using the velocity anomalies (the total velocity minus its annual mean) and the annual mean velocity (Figure 12). The percentage differences between SMOOTH and ROUGH in eddy scales in the ocean interior of the deep basin are significantly reduced (from ~40% to ~20%) when the eddy scales are diagnosed using velocity anomalies (Figure 12c). This reduction in eddy scale difference can be explained by the differences in the scales of the mean flow between the two experiments above the rough topography in the deep basin (Figure 12f). The percentage differences in eddy scales close to the bottom topography on the slope, on the other hand, remain largely unchanged between SMOOTH and ROUGH when the eddy scales are diagnosed using velocity anomalies (Figure 12c).

Previous studies also found the inclusion of rough topography can modify the mean flow path (e.g., de Marez et al., 2020; Zhang & Nikurashin, 2020). This influence of the rough topography on mean flow may further affect the eddy energy, since the eddies are mainly generated through instabilities of the mean flow. In addition, the weakening of the deep western boundary current affects the transport of deep water, which has implications for water exchange between the SCS and the northwestern Pacific (Zhou et al., 2017).

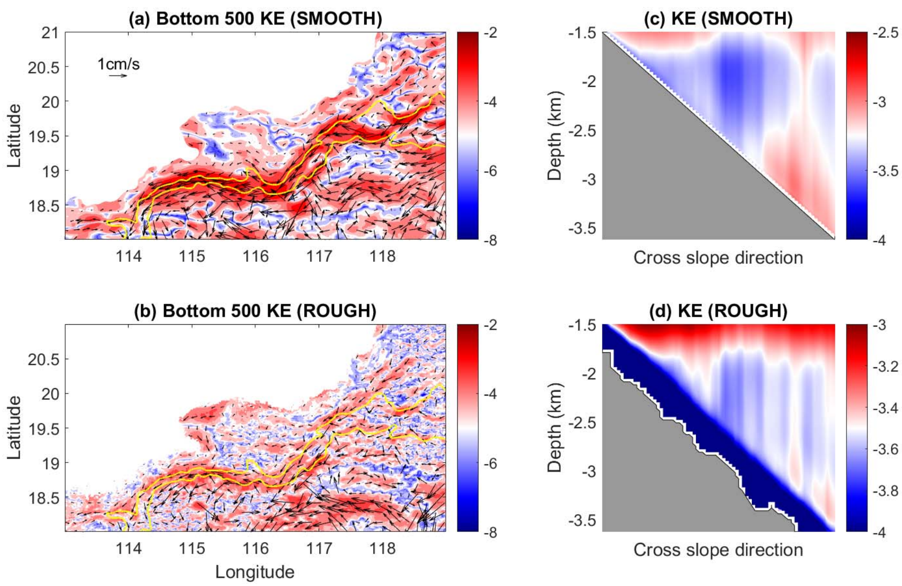

Figure 11. (a-b) Depth-averaged (bottom 500 m) kinetic energy (shading; in $\log_{10}$; m^2/s^2) and current (arrows; m/s). The two yellow lines represent 3000- and 3500-m isobaths. (c-d) Composite distribution of kinetic energy (in $\log_{10}$; m^2/s^2). Only kinetic energy below 1500 m depth is shown.

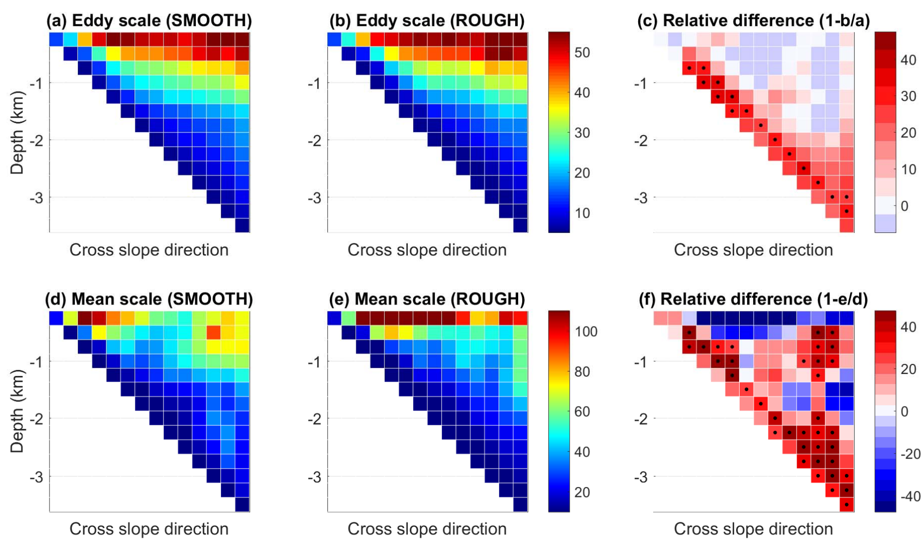

Figure 12. (a-b) Composite eddy scales (Eq. (2), km) calculated using velocity anomalies in SMOOTH and ROUGH (km) and (c) their relative differences (percentage). (d-e) Composite mean flow scales (Eq. (2), km) calculated using annual mean velocities in SMOOTH and ROUGH and (f) their relative differences (percentage). Black dots in c and f indicate percentage differences greater than 25%.

d. Contributions to the scale reduction

This reduction in bottom eddy scales is mainly contributed by three processes: wave generation due to flow interaction with rough topography and subsequent wave propagation into the ocean interior, forward energy cascade associated with processes such as nonpropagating form drag effect, and the influence of small-scale topography on the deep boundary current. Here we try to quantify the contribution of each process.

We define two regions according to the location of the deep boundary current: shallow region (500-2500 m) and deep region (deeper than 2500 m) and calculate the total/nonwave eddy scales averaged in the bottom 500 m in the two regions. In both regions, we find the nonwave eddy scale differences in the two experiments (~3 km for both regions) account for about two-thirds of the total scale differences (~5 km for both regions), indicating the wave processes can explain about one-third of the eddy scale reduction above the rough bottom. In the shallow region, the remaining two-thirds is associated with the nonwave processes and in the deep region, the modification of deep boundary current also contributes. However, we note it’s difficult to separate their contributions, since they may interact with each other. Preliminary analyses suggest the nonwave processes may be more important. For example, the nonwave scale reduces by ~20% in the shallow region (15.1 km vs. 12.0 km), but the nonwave scale reduction doesn’t increase significantly (~30%, 9.9 km vs. 6.9 km) after adding the contribution of deep boundary current in the deep region. Here we only consider the reduction of bottom eddy scales, the modification of deep boundary current could be more important in the basin interior, since the other two effects mainly occur close to the rough bottom.

e. Eddy anisotropy

Previous studies (e.g., Stewart et al., 2015) have noted that eddies tend to align with isobaths and are anisotropic particularly near the seafloor. Here we compare the eddy anisotropy in SMOOTH and ROUTH.

Following Stewart et al. (2015), the eddy anisotropy is defined here as the ratio of L/K, with $L = \sqrt{\frac{\left(\overline{u'^2} - \overline{v'^2}\right)^2}{4} + \overline{u'v'}^2}$ and $K = \frac{\overline{u'^2} + \overline{v'^2}}{2}$, where the overbars denote the annual mean and the primes deviations thereof. This ratio is in the range of 0-1 and the eddy anisotropy is stronger when this ratio is close to 1.

We find the anisotropy ratios increase with depth in both experiments (consistent with Stewart et al., 2015) but the difference between the two experiments is small and not significant (not shown).

5. Summary

The effect of small-scale topography in modulating eddy scales in the northern SCS is investigated using a high-resolution nested model conducted with either a smooth topography or a synthetic rough topography. It is found that the surface eddy scales remain unchanged after adding small-scale topography and both experiments exhibit a similar seasonal cycle associated with submesoscale generation in winter. The lack of influence of small-scale topography on surface eddy scales in the northern SCS is likely due to the strong upper ocean stratification in this region as well as the compensation effect between reduced bottom friction and enhanced viscous dissipation in ROUGH.

On the other hand, the presence of small-scale topography leads to a significant reduction of bottom eddy scales by 30-40% within hundreds meters above the rough topography in the slope region and more than 1000 m above the rough topography in the deep basin. There are three main contributions to this reduction in the diagnosed bottom eddy scales. First, part of this reduction can be explained by small-scale wave motions generated by flow interaction with rough topography and the subsequent upward wave propagation into the ocean interior. Second, topography-induced nonwave processes such as submesoscale instabilities and nonpropagating form drag effect transfer energy to small-scale balanced eddy motions via a forward energy cascade. Third, the presence of small-scale topography is found to modify the path and structure of the deep western boundary current in the northern SCS. The deep boundary current is narrower and less continuous in rough topography experiment which contributes to the reduction of diagnosed eddy scales, particularly in the deep basin interior.

The eddy length scale is a key parameter of ocean eddies and it matters for the role of the eddies play in the ocean such as in transporting, mixing tracers and eddy dissipation coefficients. As such, it is one of the key ingredients in the development of eddy parameterization schemes (e.g., Eden and Greatbatch, 2008; Visbeck et al., 1997). The results presented in this study highlight the importance of small-scale topography in modulating eddy length scales particularly in the deep ocean.

Acknowledgments

ZY and ZJ are supported by Science and Technology Innovation Foundation of Laoshan Laboratory (No. LSKJ202202501), Taishan Scholar Funds (tsqn201909052), Qingdao applied research project. The research presented in this paper was carried out on the High Performance Computing Cluster supported by National Supercomputer Center in Tianjin. We thank the three anonymous reviewers for their helpful comments that led to significant improvement of this manuscript.

Open Research

The model configuration files are available online (https://doi.org/10.7910/DVN/M2QSGG).

APPENDIX A
Synthetically-generated rough topography

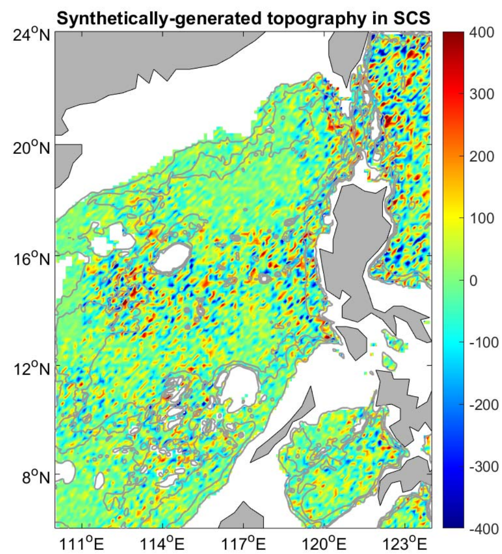

Figure A1. Synthetically small-scale (<20 km) topography in the SCS (shading, m). Gray lines represent the 1000 m, 2000 m and 3000 m isolines, respectively.

APPENDIX B
Surface CSF in C1

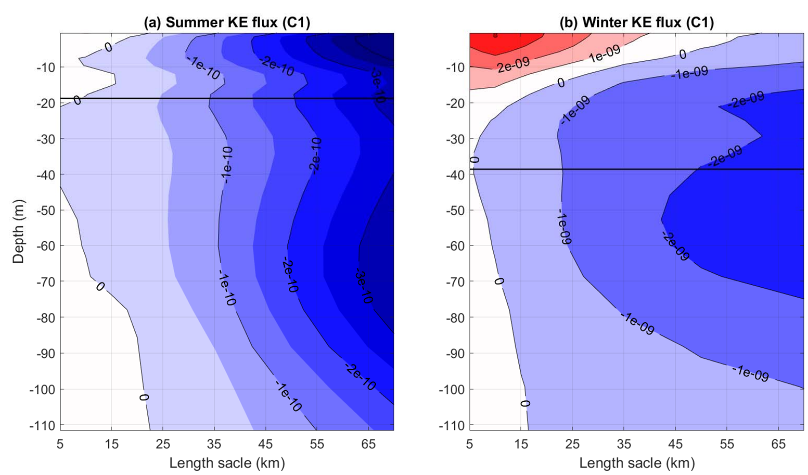

Figure B1. Time-mean surface cross-scale kinetic energy fluxes ($\Pi(\ell)$, W/kg) in (a) summer and (b) winter of C1. Positive (Negative) shading indicates a forward (inverse) energy cascade. Black lines represent the mixed layer depth (the depth with a temperature difference of 0.2^{o}C from the surface). Black lines show the locations of the mixed layer (0.2^{o}C temperature difference with surface).

APPENDIX C
Nonwave eddy scale difference between SMOOTH and ROUGH

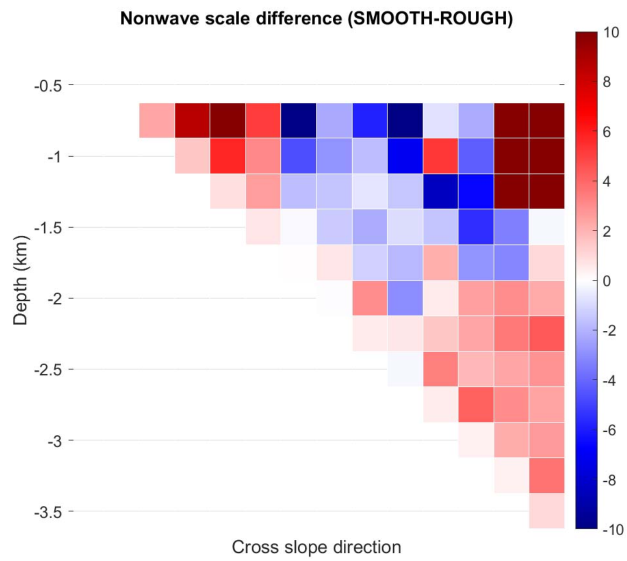

Figure C1. The nonwave eddy scale differences between the two experiments (i.e., Figure 7b minus Figure 7e, km).

References

Aluie, H., Hecht, M., & Vallis, G. K. (2018). Mapping the energy cascade in the North Atlantic Ocean: The coarse-graining method. *Journal of Physical Oceanography*. https://doi.org/10.1175/JPO-D-17-0100.1

Arbic, B. K., & Flierl, G. R. (2004). Baroclinically unstable geostrophic turbulence in the limits of strong and weak bottom Ekman friction: Application to midocean eddies. *Journal of Physical Oceanography*. https://doi.org/10.1175/1520-0485(2004)034<2257:BUGTIT>2.0.CO;2

Arbic, B. K., Polzin, K. L., Scott, R. B., Richman, J. G., & Shriver, J. F. (2013). On eddy viscosity, energy cascades, and the horizontal resolution of gridded satellite altimeter products. *Journal of Physical Oceanography*. https://doi.org/10.1175/JPO-D-11-0240.1

Baker, L. E., & Mashayek, A. (2021). Surface reflection of bottom generated oceanic lee waves. *Journal of Fluid Mechanics*, 924, A17. https://doi.org/10.1017/jfm.2021.627

Becker, J. J., Sandwell, D. T., Smith, W. H. F., Braud, J., Binder, B., Depner, J., et al., (2009). Global Bathymetry and Elevation Data at 30 Arc Seconds Resolution: SRTM30_PLUS. *Marine Geodesy*. https://doi.org/10.1080/01490410903297766

Bell, T. H. (1975a). Lee waves in stratified flows with simple harmonic time dependence. *Journal of Fluid Mechanics*. https://doi.org/10.1017/S0022112075000560

Bell, T. H. (1975b). Topographically generated internal waves in the open ocean. *Journal of Geophysical Research*. https://doi.org/10.1029/jc080i003p00320

Capet, X., McWilliams, J. C., Molemaker, M. J., & Shchepetkin, A. F. (2008). Mesoscale to submesoscale transition in the California current system. Part III: Energy balance and flux. *Journal of Physical Oceanography*. https://doi.org/10.1175/2008JPO3810.1

de Marez, C., Lahaye, N. J., & Gula, J. (2020). Interaction of the Gulf Stream with small scale topography: a focus on lee waves. *Scientific Reports*. https://doi.org/10.1038/s41598-020-59297-5

Dong, J., Fox-Kemper, B., Zhang, H., & Dong, C. (2020). The Seasonality of Submesoscale Energy Production, Content, and Cascade. *Geophysical Research Letters*, 47(6), 1-9. https://doi.org/10.1029/2020GL087388

Eden, C., & Greatbatch, R. J. (2008). Diapycnal mixing by meso-scale eddies. *Ocean Modelling*. https://doi.org/10.1016/j.ocemod.2008.04.006

Eyink, G. L., & Aluie, H. (2009). Localness of energy cascade in hydrodynamic turbulence. I. smooth coarse graining. *Physics of Fluids*. https://doi.org/10.1063/1.3266883

Goff, J. A., & Jordan, T. H. (1988). Stochastic modeling of seafloor morphology: inversion of Sea Beam data for second-order statistics. *Journal of Geophysical Research*. https://doi.org/10.1029/jb093ib11p13589

Hurlburt, H. E., & Hogan, P. J. (2008). The Gulf Stream pathway and the impacts of the eddy-driven abyssal circulation and the Deep Western Boundary Current. *Dynamics of Atmospheres and Oceans*, 45(3–4), 71–101. https://doi.org/10.1016/j.dynatmoce.2008.06.002

Klymak, J. M. (2018). Nonpropagating form drag and turbulence due to stratified flow over large-scale Abyssal Hill Topography. *Journal of Physical Oceanography*. https://doi.org/10.1175/JPO-D-17-0225.1

Kunze, E., & Lien, R.-C. (2019). Energy sinks for lee waves in shear flow. *Journal of Physical Oceanography*, 49(11), 2851‑2865. https://doi.org/10.1175/jpo-d-19-0052.1

Marshall, J., Adcroft, A., Hill, C., Perelman, L., & Heisey, C. (1997). A finite-volume, incompressible navier stokes model for, studies of the ocean on parallel computers. *Journal of Geophysical Research: Oceans*. https://doi.org/10.1029/96JC02775

Melet, A., Nikurashin, M., Muller, C., Falahat, S., Nycander, J., Timko, P. G., et al. (2013). Internal tide generation by abyssal hills using analytical theory. *Journal of Geophysical Research: Oceans*, 118(11), 6303‑6318. https://doi.org/10.1002/2013JC009212

Nagai, T., Tandon, A., Kunze, E., & Mahadevan, A. (2015). Spontaneous generation of near-inertial waves by the Kuroshio Front. *Journal of Physical Oceanography*. https://doi.org/10.1175/JPO-D-14-0086.1

Naveira Garabato, A. C., Yu, X., Callies, J., Barkan, R., Polzin, K. L., Frajka-Williams, E. E., et al. (2022). Kinetic Energy Transfers between Mesoscale and Submesoscale Motions in the Open Ocean's Upper Layers. *Journal of Physical Oceanography*, 52(1), 75–97. https://doi.org/10.1175/JPO-D-21-0099.1

Nikurashin, M., & Ferrari, R. (2010). Radiation and dissipation of internal waves generated by geostrophic motions impinging on small-scale topography: Theory. *Journal of Physical Oceanography*, 40(5), 1055‑1074. https://doi.org/10.1175/2009JPO4199.1

Nikurashin, M., & Legg, S. (2011). A mechanism for local dissipation of internal tides generated at rough topography. *Journal of Physical Oceanography*, 41(2), 378‑395. https://doi.org/10.1175/2010JPO4522.1

Nikurashin, M., Vallis, G. K., & Adcroft, A. (2013). Routes to energy dissipation for geostrophic flows in the Southern Ocean. *Nature Geoscience*. https://doi.org/10.1038/ngeo1657

Polzin, K. L., Toole, J. M., Ledwell, J. R., & Schmitt, R. W. (1997). Spatial variability of turbulent mixing in the abyssal ocean. *Science*, 276(5309), 93‑96. https://doi.org/10.1126/science.276.5309.93

Qiu, B., Chen, S., Klein, P., Sasaki, H., & Sasai, Y. (2014). Seasonal mesoscale and submesoscale eddy variability along the north pacific subtropical countercurrent. *Journal of Physical Oceanography*. https://doi.org/10.1175/JPO-D-14-0071.1

Rhines, P. B. (1975). Waves and turbulence on a beta-plane. *Journal of Fluid Mechanics*. https://doi.org/10.1017/S0022112075001504

Ruan, X., Wenegrat, J. O., & Gula, J. (2021). Slippery Bottom Boundary Layers: The Loss of Energy From the General Circulation by Bottom Drag. *Geophysical Research Letters*, 48(19). https://doi.org/10.1029/2021GL094434

Saenko, O. A., Zhai, X., Merryfield, W. J., & Lee, W. G. (2012). The combined effect of tidally and eddy-driven diapycnal mixing on the large-scale ocean circulation. *Journal of Physical Oceanography*. https://doi.org/10.1175/JPO-D-11-0122.1

Salmon, R. (1998). Lectures on Geophysical Fluid Dynamics. *Lectures on Geophysical Fluid Dynamics*. https://doi.org/10.1093/oso/9780195108088.001.0001

Sasaki, H., Klein, P., Qiu, B., & Sasai, Y. (2014). Impact of oceanic-scale interactions on the seasonal modulation of ocean dynamics by the atmosphere. *Nature Communications*, 5, 1–8. https://doi.org/10.1038/ncomms6636

Schubert, R., Gula, J., Greatbatch, R. J., Baschek, B., & Biastoch, A. (2020). The submesoscale kinetic energy cascade: Mesoscale absorption of submesoscale mixed layer eddies and frontal downscale fluxes. *Journal of Physical Oceanography*. https://doi.org/10.1175/JPO-D-19-0311.1

Shakespeare, C. J., & Hogg, A. M. C. (2017). Spontaneous surface generation and interior amplification of internal waves in a regional-scale ocean model. *Journal of Physical Oceanography*. https://doi.org/10.1175/JPO-D-16-0188.1

Srinivasan, K., McWilliams, J. C., Molemaker, M. J., & Barkan, R. O. Y. (2019). Submesoscale vortical wakes in the lee of topography. *Journal of Physical Oceanography*. https://doi.org/10.1175/JPO-D-18-0042.1

Stammer, D. (1997). Global characteristics of ocean variability estimated from regional TOPEX/POSEIDON altimeter measurements. *Journal of Physical Oceanography*. https://doi.org/10.1175/1520-0485(1997)027<1743:GCOOVE>2.0.CO;2

Stewart, K. D., Spence, P., Waterman, S., Sommer, J. Le, Molines, J. M., Lilly, J. M., & England, M. H. (2015). Anisotropy of eddy variability in the global ocean. *Ocean Modelling*, 95, 53‑65. https://doi.org/10.1016/j.ocemod.2015.09.005

Sun, H., Yang, Q., Zheng, K., Zhao, W., Huang, X., & Tian, J. (2022). Internal lee waves generated by shear flow over smallscale topography. *Journal of Geophysical Research: Oceans*, 127, e2022JC018547. https://doi.org/10.1029/2022JC018547

Torres, H. S., Klein, P., Menemenlis, D., Qiu, B., Su, Z., Wang, J., et al. (2018). Partitioning Ocean Motions Into Balanced Motions and Internal Gravity Waves: A Modeling Study in Anticipation of Future Space Missions. *Journal of Geophysical Research: Oceans*, 123(11), 8084–8105. https://doi.org/10.1029/2018JC014438

Trossman, D. S., Arbic, B. K., Straub, D. N., Richman, J. G., Chassignet, E. P., Wallcraft, A. J., & Xu, X. (2017). The role of rough topography in mediating impacts of bottom drag in eddying ocean circulation models. *Journal of Physical Oceanography*. https://doi.org/10.1175/JPO-D-16-0229.1

Trossman, D. S., Waterman, S., Polzin, K. L., Arbic, B. K., Garner, S. T., Naveira Garabato, A. C., & Sheen, K. L. (2015). Internal lee wave closures: Parameter sensitivity and comparison to observations. *Journal of Geophysical Research*, 120, 7997–8019. https://doi.org/10.1002/2015jc010892

Visbeck, M., Marshall, J., Haine, T., & Spall, M. (1997). Specification of eddy transfer coefficients in coarse-resolution ocean circulation models. *Journal of Physical Oceanography*. https://doi.org/10.1175/1520-0485(1997)027<0381:SOETCI>2.0.CO;2

Wang, S., Jing, Z., Zhang, Q., Chang, P., Chen, Z., Liu, H., & Wu, L. (2019). Ocean eddy energetics in the spectral space as revealed by high-resolution general circulation models. *Journal of Physical Oceanography*, 49(11), 2815 – 2827. https://doi.org/10.1175/JPO-D-19-0034.1

Whalen, C. B., de Lavergne, C., Naveira Garabato, A. C., Klymak, J. M., MacKinnon, J. A., & Sheen, K. L. (2020). Internal wave-driven mixing: governing processes and consequences for climate. *Nature Reviews Earth and Environment*. https://doi.org/10.1038/s43017-020-0097-z

Wu, Y., Kunze, E., Tandon, A., & Mahadevan, A. (2022). Reabsorption of Lee-Wave Energy in Bottom-Intensified Currents. *Journal of Physical Oceanography*. https://doi.org/10.1175/jpo-d-22-0058.1

Yang, Z., Wang, G., & Chen, C. (2019). Horizontal velocity structure of mesoscale eddies in the South China Sea. *Deep-Sea Research Part I: Oceanographic Research Papers*. https://doi.org/10.1016/j.dsr.2019.06.001

Yang, Z., Jing, Z., & Zhai, X. (2022). Effect of Small-Scale Topography on Eddy Dissipation in the Northern South China Sea. *Journal of Physical Oceanography*, 52(10), 2397–2416. https://doi.org/10.1175/JPO-D-21-0208.1

Yang, Z., Jing, Z., & Zhai, X. (2023). Energy sinks for lee waves in the Northern South China Sea. *Journal of Geophysical Research: Oceans*. 128, e2022JC019060. https://doi.org/10.1029/2022JC019060

Yang, Z., Zhai, X., Marshall, D. P., & Wang, G. (2021). An Idealized Model Study of Eddy Energetics in the Western Boundary “Graveyard”. *Journal of Physical Oceanography*. https://doi.org/10.1175/jpo-d-19-0301.1

Zhang, J., Zhang, Z., Qiu, B., Zhang, X., Sasaki, H., Zhao, W., & Tian, J. (2021). Seasonal Modulation of Submesoscale Kinetic Energy in the Upper Ocean of the Northeastern South China Sea. *Journal of Geophysical Research: Oceans*, 126(11). https://doi.org/10.1029/2021JC017695

Zhang, X., & Nikurashin, M. (2020). Small-Scale Topographic Form Stress and Local Dynamics of the Southern Ocean. *Journal of Geophysical Research: Oceans*. https://doi.org/10.1029/2019JC015420

Zhang, Z., Zhang, Y., Qiu, B., Sasaki, H., Sun, Z., Zhang, X., et al., (2020). Spatiotemporal Characteristics and Generation Mechanisms of Submesoscale Currents in the Northeastern South China Sea Revealed by Numerical Simulations. *Journal of Geophysical Research: Oceans*. https://doi.org/10.1029/2019JC015404

Zhao, X., Zhou, C., Xu, X., Ye, R., & Zhao, W. (2020). Deep circulation in the South China Sea simulated in a regional model. *Ocean Dynamics*. https://doi.org/10.1007/s10236-020-01411-2

Zhou, C., Zhao, W., Tian, J., Zhao, X., Zhu, Y., Yang, Q., & Qu, T. (2017). Deep Western Boundary Current in the South China Sea. *Scientific Reports*, *7*(1), 1–7. https://doi.org/10.1038/s41598-017-09436-2